Ceramics International xxx (xxxx) xxx

Contents lists available at ScienceDirect

Ceramics International

journal homepage: www.elsevier.com/locate/ceramint

Investigating the strength of Ti/TiB interfaces at multiple scales using density functional theory, molecular dynamics, and cohesive zone modeling

Siamak Attarian *, Shaoping Xiao

Department of Mechanical Engineering, University of Iowa Technology Institute, The University of Iowa, Iowa City, IA, 52242, USA

ARTICLE INFO

Keywords:
Metal matrix composite
Metal/ceramic interface
Cohesive zone modeling
Stacking fault energies
Molecular dynamics simulations

ABSTRACT

Titanium/titanium boride (Ti/TiB) composites are interesting technological materials with prospective applications in the aerospace, automotive, and biomedical industries. However, not much has been studied about the failure mechanisms of these composites. This article thoroughly investigates the adhesion and strength of two well-known Ti/TiB interface variants formed during the production of Ti/TiB composites below and above 910 °C, respectively. The studies were carried out using different theoretical methods at multiple scales, including density functional theory (DFT), molecular dynamics (MD), cohesive zone modeling (CZM), and the finite element method (FEM). First, we employed DFT to investigate the interfacial adhesion and strength of the selected planes. Then, MD simulations were utilized to study the misfit dislocation networks and derive interfacial CZMs for FEM modeling and simulation of composites. Our FEM simulations showed that the Ti/TiB interface has sufficient strength to transfer the shear load from Ti to TiB without debonding at room temperature. The results have confirmed the same phenomenon observed in some experimental studies and interpreted this phenomenon from a multiscale point of view. The research findings can be used in quantifying the failure stress of TiB whiskers directly from tension tests on Ti/TiB composites by ruling out the possibility of interface debonding.

1. Introduction

Titanium (Ti) and its alloys are the materials of choice when there is a need for high specific strength or chemical resistance. However, they have low elastic modulus and wear resistance, limiting their application. Reinforcing these materials with inclusions and creating titanium matrix composites (TMCs) can improve these deficiencies, enhance their high-temperature strength, and make them candidates for a wide range of applications from high-speed intercept missiles [1] to biomedical applications [2]. Various inclusions are used to produce TMCs, including titanium carbide (TiC) [3], titanium boride (TiB) [4], titanium nitride (TiN) [5], silicon carbide (SiC) [6], graphene [7], aluminum oxide (Al_2O_3) [8], etc. Titanium boride has similar thermal expansion and density to titanium, resulting in low thermal stresses during manufacturing and property enhancement of Ti without increasing its density. In addition, TiB is biocompatible [9], and its elastic modulus is four times higher than commercially pure titanium. The microstructure of Ti/TiB composites can be tailored to form a two-scale network to achieve superior mechanical properties, compared to the conventionally manufactured composites [10]. Such characteristics have made Ti/TiB composite a promising material for use in the aerospace [11], automotive [12], and biomedical industries [13], especially at high temperatures.

Titanium boride is a ceramic with high hardness and stiffness, but it does not naturally exist in a pure form. It can be produced during an in situ reaction between titanium and a compound that contains boron, such as titanium diboride (TiB_2): $Ti + TiB_2 \rightarrow 2TiB$. This reaction produces single crystal TiB whiskers or short fibers [14], mainly in micro-length scales. A common observation in experimental studies regarding the growth of TiB within Ti (either α-Ti or β-Ti) is that TiB grows faster in the [010] direction, which leads to its whisker shape [15–17]. A few orientation relationships (ORs) have also been reported for α-Ti/TiB interfaces, but the following have been mentioned frequently in the literature: $(100)_{TiB} \parallel (10\bar{1}0)_{\alpha-Ti}$ [15,18–20] and $(001)_{TiB} \parallel (0001)_{\alpha-Ti}$ [4,19,21–23], both of which have a $[010]_{TiB} \parallel$

* Corresponding author.
E-mail address: siamak-attarian@uiowa.edu (S. Attarian).

https://doi.org/10.1016/j.ceramint.2022.07.259
Received 2 June 2022; Received in revised form 9 July 2022; Accepted 21 July 2022
Available online 6 August 2022

$[11\bar{2}0]_{\alpha-Ti}$ relationship. Throughout this text, we refer to $(100)_{TiB} \parallel (10\bar{1}0)_{\alpha-Ti}$ as OR1 and $(001)_{TiB} \parallel (0001)_{\alpha-Ti}$ as OR2. Also, from here on, all the coordinates are in the local coordinates of TiB.

Titanium boride is not readily available, and it is difficult to investigate its properties. The mechanical and thermal properties of TiB have been investigated via either density functional theory (DFT) [24,25] or indirect experimental methods. In experiments [26,27], after a specific property of Ti/TiB composite was measured, the same property could be estimated for TiB through averaging methods. Although the averaging methods may provide enough accuracy for calculating properties such as the elastic modulus of TiB, they do not apply to computing failure stresses (e.g., yield or ultimate stress). This is because, in addition to the failure stress of Ti and TiB, the strength of the Ti/TiB interface also plays an important factor that is not considered by the averaging methods.

The interface between TiB and Ti has been qualitatively described as clean and flat [15,28–30] with a low lattice mismatch and categorized as a semi-coherent interface. Such a description may suggest it is a strong interface. However, one cannot quantify the actual strength of the interface without experiments such as a pull-out test [31,32], a micro-pillar test [33], or computational simulations at the atomic scales. To the best of the authors' knowledge, there are no experimental works on testing the strength of Ti/TiB interfaces. On the other hand, a few recent computational studies have investigated some aspects of Ti/TiB interfaces via DFT. Nandwana et al. [34] used DFT calculations to compare OR1 and $(101)_{TiB} \parallel (10\bar{1}0)_{\alpha-Ti}$ interfaces. They found that the former has a lower interfacial energy than the latter, so TiB prefers to make the former interface. However, they considered only one of the variations of OR1 interfaces in their work. It shall be noted that the variations/terminations of Ti/TiB interfaces will be discussed in Section 2. Fan et al. [35] compared the formation energies and the work of separation of OR1 with four different terminations of $(100)_{TiB}$ and four different stackings of OR1 (16 interfaces overall). They found that one of the examined interfaces has noticeably lower formation energy and higher separation work than the others. This interface is viewed as the most energetically favorable and thermodynamically stable interface, and it is most likely to form in real situations. Zhang et al. [36] did a similar study and examined the adhesive work and interface energy of eight variations of OR1 and determined the variation with the lowest interfacial energy, which creates the most stable interface. Their results agreed with the findings of Fan et al. [35]. In another work, An et al. [37] performed a combined experimental and theoretical study of TiB whiskers formed in Ti6Al4V, an α-β alloy of titanium. They identified two interfaces forming between TiB and α-Ti and two interfaces between TiB and β-Ti. Then, they performed a thorough DFT analysis of the energetics of the interfaces with different terminations. They showed that all the examined interfaces have high adhesion strength. However, among them, the coherent $(100)_{TiB} \parallel (\bar{1}21)_{\beta-Ti}$ interface is stronger than the semi coherent $(\bar{2}01)_{TiB} \parallel (0001)_{\alpha-Ti}$ interface. It is worth mentioning that we are unaware of any prior theoretical studies on OR2.

The above summarizes the current state of our knowledge on α-Ti/TiB interfaces. In this paper, we conduct a comprehensive study on both OR1 and OR2 by quantifying the strength of the interface at various scales as follows. In Section 2, we explain the applications of DFT to obtain the generalized stacking fault energies (GSFE) and the work of adhesion (WOA) of both OR1 and OR2 to get insights into the relative strength of each interface and the layers close to it. In Section 3, we discuss the misfit dislocation networks and their influence on the behavior of the interfaces via molecular dynamics (MD) simulations. Shear and tensile tests are performed in Section 4 via MD simulations to quantify the strength of the interfaces at room temperature and develop cohesive zone models (CZM). In Section 5, the developed CZMs are used in conjunction with the finite element method (FEM) to assess the failure of Ti/TiB composites at room temperature, and the results are discussed. We present an in-depth discussion in Section 6 and conclude the research in Section 7.

2. Studies of the interfaces by DFT

2.1. Methodology to obtain GSFE and WOA

Density functional theory simulations have been frequently used to study metal/ceramic interfaces. Usually, GSFE curves are obtained to assess the behavior of the interface subject to shear deformation. These curves are indicators of the energy barrier to slip between two surfaces. Meanwhile, WOA, the amount of energy needed to separate an interface into two surfaces, is calculated to evaluate the interfacial adhesion. Several metal/ceramic interfaces have been studied by means of DFT simulations, including Ti/CrN, Cr/VN, Cu/TiN [38], Ag/MgO [39], Ti/TiN [40], Al/TiC [41], etc.

The first thing that one needs to know is which variation of the experimentally observed Ti/TiB OR is likely to happen. The minimum interfacial energy is used to determine the most thermodynamically stable variant. Fig. 1 shows TiB's [100] and [001] surfaces. Fig. 1(a) indicates four terminations of the TiB unit cell that could be considered as the [100] surface. There is no experimental evidence to clarify which termination is in contact with the Ti surface. However, previous DFT works [35,36] indicated that the B1 termination (Fig. 1(a)) in OR1 creates the most stable interface, so it is the only termination we consider for OR1. On the other hand, there are two possible terminations of the [001] surface, as shown in Fig. 1(b). For OR2, we examine both BT1 and BT2 as TiB's [001] surfaces (Fig. 1(b)) to find which one has lower interfacial energy, and we use that termination for the studies in this paper.

The minimum number of atomic layers to yield accurate results is chosen by modeling different columnar cells with increasing layers until the calculated surface energy converges. In another work, Fan et al. [35] reached enough accuracy with nine layers of Ti and eight layers of TiB for OR1. Although more layers can result in higher accuracy, the gain is insignificant. In this study, we use 20 layers of Ti and 24 layers of TiB for OR1, and 10 layers of Ti, and 16 layers of TiB for OR2. It should be noted that each elevation that contains atoms (whether a single atom or double atoms) is considered a layer. This definition is consistent with the work of Fan et al. [35]. In addition, choosing the layer numbers mentioned above was practical, and we wanted each columnar cell of OR1 and OR2 to have the same number of atoms (44 atoms). Due to the lattice mismatch between Ti and TiB unit cells, the Ti unit cell was stretched or contracted to become the same size as the TiB lattice. A 15 Å vacuum layer has been put on the top of the columnar cell to avoid the interaction of atoms across the periodic boundary in the vertical direction. Figs. 2 and 3 show the modeling process of OR1 and OR2.

After constructing the columnar cells, we needed to know the Ti layer's energetically favorable stacking (positioning) on top of the TiB layer. To address this question, we conducted a grid search in which the Ti layer was placed on different points of an 11 × 11 grid, as illustrated in Fig. 4. The total energy of the system was calculated after relaxation at each stacking. The columnar cell was fixed during the relaxation, and the atoms were allowed to relax only in the vertical direction. After finding the grid point with the minimum energy, this configuration was fully relaxed with respect to the columnar cell dimensions and atomic positions. It should be noted that the choice of the 11 × 11 grid is arbitrary, and the energies calculated on these points are used to determine the region with the minimum potential energy only. Later, by fully relaxing the system in that region, the system finds its energetically favorable state after minor adjustment of the atomic positions. The resulting cell and atomic positions were used as the initial configuration for GSFE and WOA calculations. All the mentioned steps were carried out for OR1 with B1 termination and for OR2 with BT1 and BT2 terminations.

The DFT calculations were performed using Quantum ESPRESSO code [42]. The projector-augmented wave (PAW) [43] method was utilized to describe the core states. In addition, the Perdew-Burke-Ernzerhof generalized gradient approximation

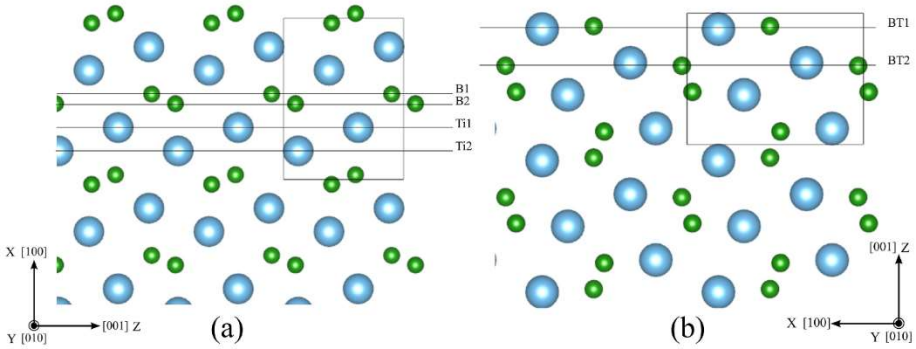

Fig. 1. Possible terminations of (a) [100] surface and (b) [001] surface of TiB.

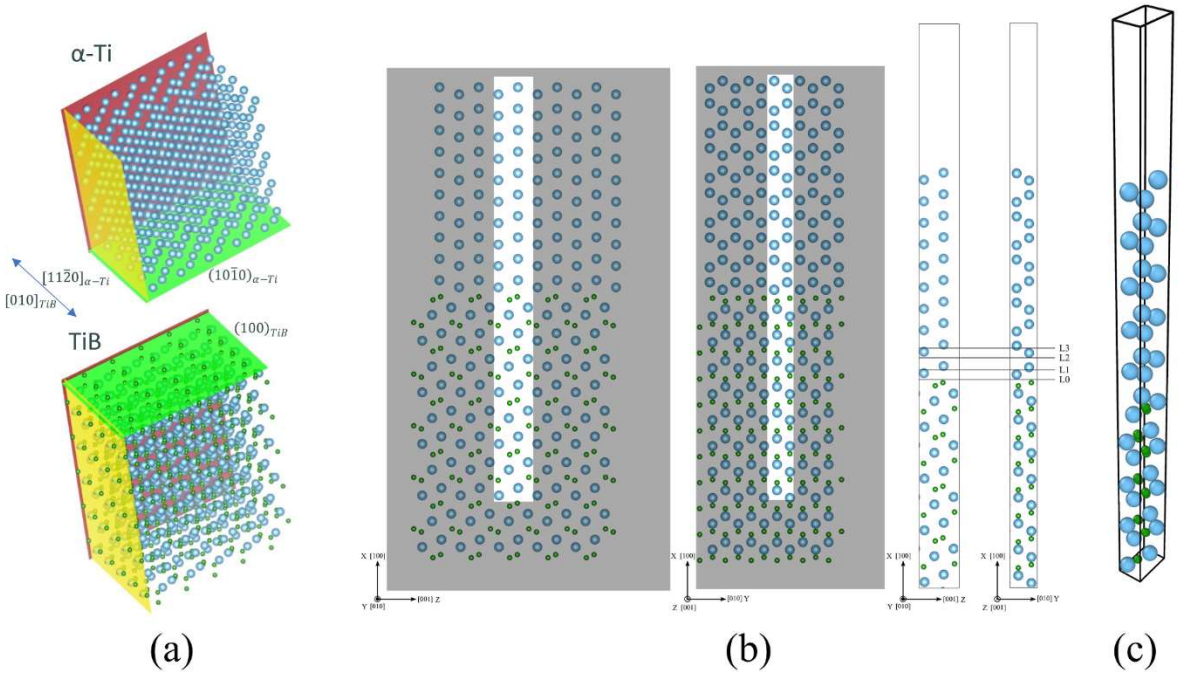

Fig. 2. Preparation of the Ti/TiB columnar cell for DFT simulations of OR1: (a) Ti and TiB are properly oriented so they would create OR1, (b) Ti is slightly deformed to become consistent with the periodicity of TiB, and (c) a columnar cell of Ti/TiB interface with periodicity in Y and Z directions is selected for DFT simulations.

(PBE-GGA) [44] was employed for the exchange and correlation functional. A cutoff energy of 585 eV (43 Ry) for the plane-wave basis set was used. In addition, k-point meshes of 1 × 4 × 4 for OR1 and 4 × 4 × 1 for OR2 were used for the grid search. For the rest of the calculations, we used 1 × 8 × 8 and 8 × 8 × 1 k-point meshes for OR1 and OR2, respectively. The chosen k-point mesh had errors less than 1 meV/atom compared to a denser mesh.

Because TiB whiskers grow in the [010] direction, only the load-bearing capacity of OR1 and OR2 in this direction is relevant to the mechanics of Ti/TiB composites in the case of resistance to shear stresses. Hence, we only calculated the GSFE curves in both interfaces' [010] direction. Considering the fact that TiB has much higher failure stress than Ti due to the strong covalent bonds, we examined only four levels of L0~L3 in the Ti cell (shown in Figs. 2 and 3) to determine which one has the least energy barrier to slip. To calculate the GSFE curve for each level, we moved the atoms above the level in the [010] direction in 10 steps. The columnar cell was fixed at each step, and the atoms were only allowed to relax in the vertical direction.

To calculate the WOA at each of L0~L3, we split the main columnar cell into two isolated columnar cells of the atoms above and below that level, respectively. Then, after letting the cells and their atoms fully relax, we used their energy to calculate the WOA of that level. Similarly, we also calculated the formation energy (interfacial energy) of the L0 level. The following equations were used for calculations of WOA and the interfacial energy, respectively [36]:

$$W_{ad} = \frac{E_{top} + E_{bottom} - E_{total}}{A} \quad \text{Eq.1}$$

$$\gamma_{int} = \frac{E_{total} - NE_{bulk,Ti} - ME_{bulk,TiB}}{A} - \gamma_{surf,Ti} - \gamma_{surf,TiB} \quad \text{Eq.2}$$

where W_{ad} is the WOA; γ_{int} is the interfacial energy. E_{top} and E_{bottom} are the energies of the isolated columnar cells above and below a level, respectively. E_{total} is the energy of the main columnar cell. A is the cross-section of the main columnar cell. $E_{bulk,Ti}$ and $E_{bulk,TiB}$ are the energies of the unit cells of Ti and TiB in their bulk forms. $\gamma_{surf,Ti}$ and $\gamma_{surf,TiB}$ are the surface energies of the exposed surfaces at the top (Ti) and bottom (TiB) of the columnar cell. N and M are the numbers of unit cells of Ti and TiB, respectively, to generate the simulated columnar cell. Each unit cell of Ti contains four atoms, and each unit cell of TiB contains eight atoms. Since each columnar cell consists of 44 atoms, N and M are 5 and 3, respectively. All the calculated energies in both equations are for fully relaxed cells.

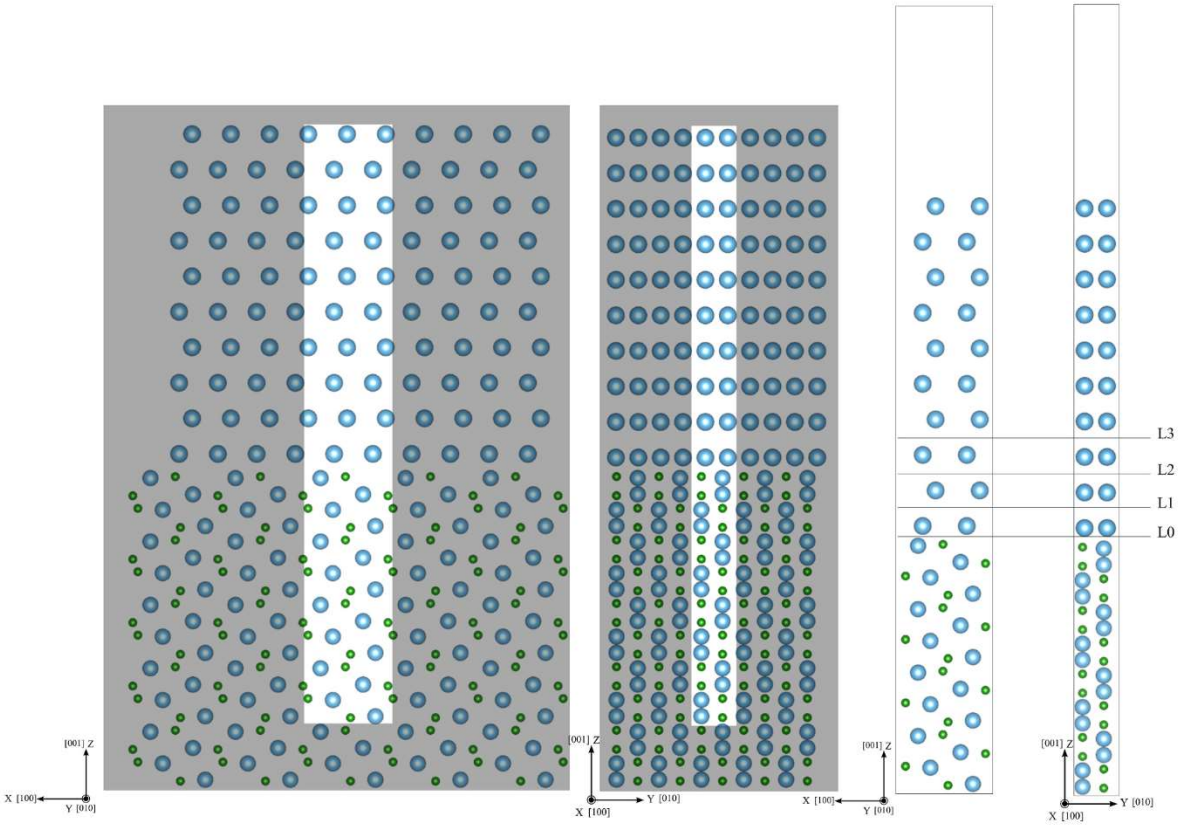

Fig. 3. A sample unit cell used for the calculations of GSFE and WOA of OR2.

2.2. Results of GSFE

Fig. 5 compares the GSFE curves of the L0~L3 levels of OR1 in the [010] direction. As the figure shows, the L0 level has the highest energy barrier against slip with the stacking fault energy of $\gamma_{[010]} = 3.69\ J/m^2$. This means that the OR1 interface at the L0 level is strongly bonded. In other words, it will not be the plane to slip when subjected to shear stress. Among the examined levels, the L2 level is the weakest with $\gamma_{[010]} = 0.45\ J/m^2$, but it is still higher than $\gamma_{[010]} = 0.24\ J/m^2$, which was obtained for <a> prismatic slip of α-Ti by Kwasniak et al. [45]. This suggests that when subjected to shear stress, the levels within α-Ti farther from the interface are prone to slipping. Here, we don't consider the effects of the misfit dislocation network at the interface; this will be discussed later.

Regarding the OR2 interface, as discussed in Section 2.1, the $(001)_{TiB}$ could be either *BT*1 or *BT*2, as shown in Fig. 1(b). Therefore, it is necessary to calculate the interface energy of each plane with the Ti layer to find the energetically favorable interface.

After obtaining the values $\gamma_{surf,Ti(0001)} = 1.95\ J/m^2$, $\gamma_{surf,TiB(001)\ BT1} = 2.91\ J/m^2$, and $\gamma_{surf,TiB(001)\ BT2} = 6.69\ J/m^2$, the interface energies were calculated to be:

$$\gamma_{int} = 3.19\ J/m^2 \text{for } (001)_{TiB\ BT1} \parallel (0001)_{\alpha-Ti} \text{and}$$

$$\gamma_{int} = 8.80\ J/m^2 \text{for} (001)_{TiB\ BT2} \parallel (0001)_{\alpha-Ti}$$

This indicates that the $(0001)_{\alpha-Ti}$ has much lower interface energy with the BT1 plane than the BT2 plane. In addition, we calculated the WOA of $(001)_{TiB\ BT2} \parallel (0001)_{\alpha-Ti}$ to be $-1.33\ J/m^2$. This suggests that extra work is needed to bring these two surfaces together, and that they are not attracted to each other naturally. Therefore, the rest of the calculations were conducted for the interface between the Ti and the BT1 plane of TiB.

Fig. 6 compares the GSFE curves of levels L0~L3 in the [010] direction of OR2. It can be seen that the L2 level has the lowest barrier against slip. The unstable stacking fault calculated by Kwasniak et al. [45] for <a> basal slip of α-Ti is $\gamma = 0.4\ J/m^2$, which is a bit higher than the L2 layer. In this case, although the L0 level is strong enough to pass the shear stress from the Ti matrix to the TiB whisker, the slip will happen eventually at the layers close to the interface.

2.3. Results of the WOA

Fig. 7 shows the WOA of levels L0~L3 of OR1. The L0 level has a very strong bonding with $W_{ad} = 6.29\ J/m^2$. The L2 level is again the weakest among the examined layers, with $W_{ad} = 3.75\ J/m^2$. This number is slightly less than the adhesive work of the $(10\bar{1}0)$ plane of α-Ti, which was measured as $4.04\ J/m^2$ (twice its surface energy of $2.02\ J/m^2$). This suggests that the existence of the interface has slightly affected the strength of that level.

The adhesive works of levels L0~L3 for OR2 are shown in Fig. 8. As the figure shows, the L1 level has very low adhesive work. Based on the value obtained for the surface energy of the (0001) plane of Ti ($1.95\ J/m^2$), the adhesive work at the layers farther from the interface could be as high as $3.9\ J/m^2$.

Overall, the results of this section show that the L0 levels (i.e., the Ti/TiB interfaces) of both OR1 and OR2 are strong enough to tolerate tensile and shear stresses until one of the levels within the Ti layer causes the failure.

3. Misfit dislocation networks

3.1. Molecular dynamics modeling of the interfaces

The Ti/TiB interface is semi-coherent, meaning that the lattice

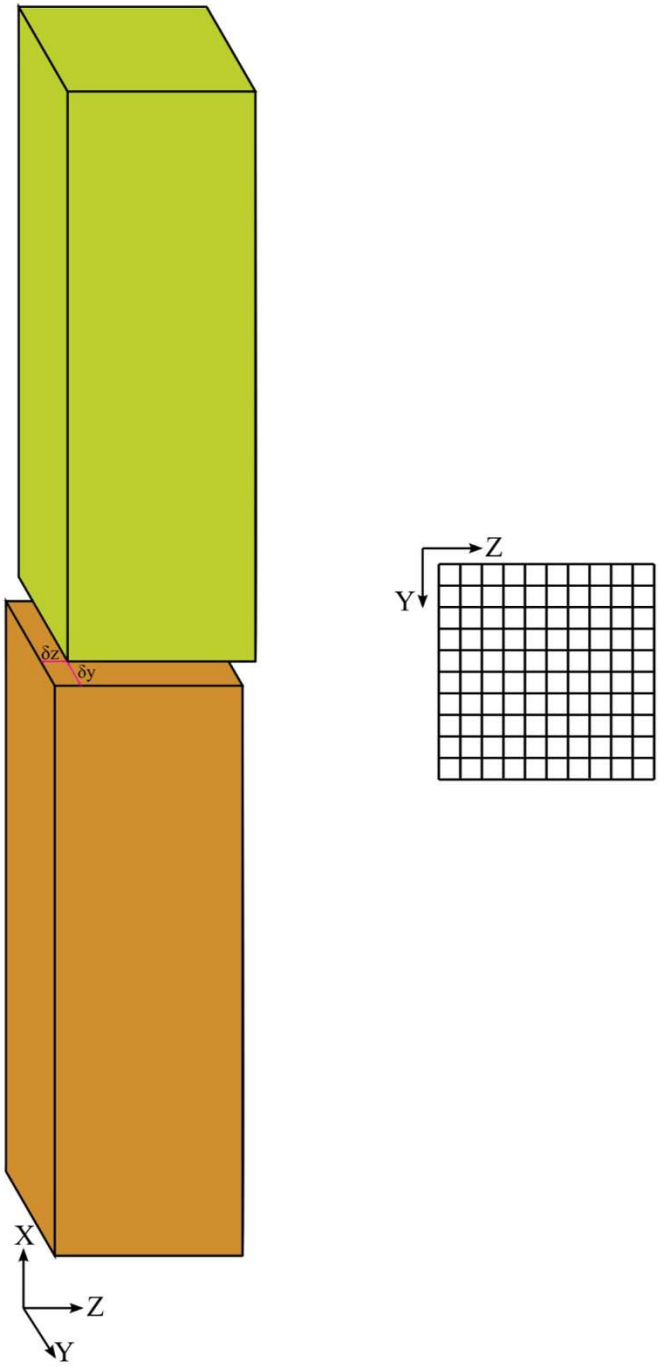

Fig. 4. Grid search for the optimal stacking of Ti on top of TiB.

constants and, hence, the periodicity of Ti and TiB are different along the interface. To study the characteristics of the interfaces via DFT in the previous section, we generated a model of a single column with periodic boundaries to represent the interface and then stretched/contracted the Ti unit cell to make the model a coherent columnar cell. Such a model has its scale limitations. Indeed, when considering the Ti/TiB interface at the molecular length scale, atoms on the interface may position differently at different locations to reach the minimum energy. This can cause some parts of the interface to behave differently from others. Usually, some regularities can be found in the appearance of the interface, which would produce a pattern called a misfit dislocation network (MDN) [46]. The misfit of the lattice constants introduces defects at the interface. The defects can be extended into the Ti layers that are close to

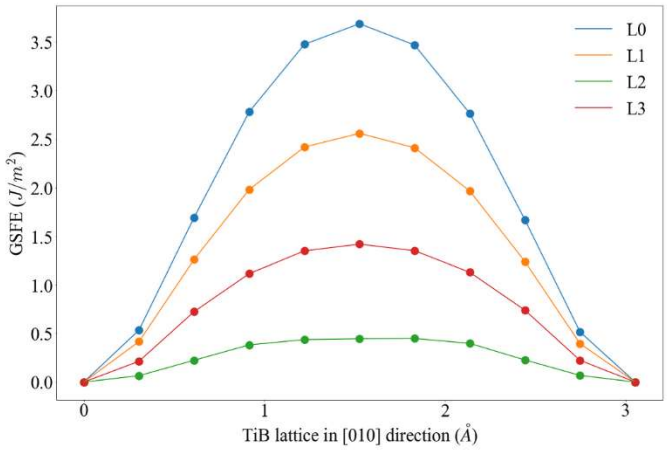

Fig. 5. Comparison of GSFE curves for levels L0~L3 of OR1 in the [010] direction.

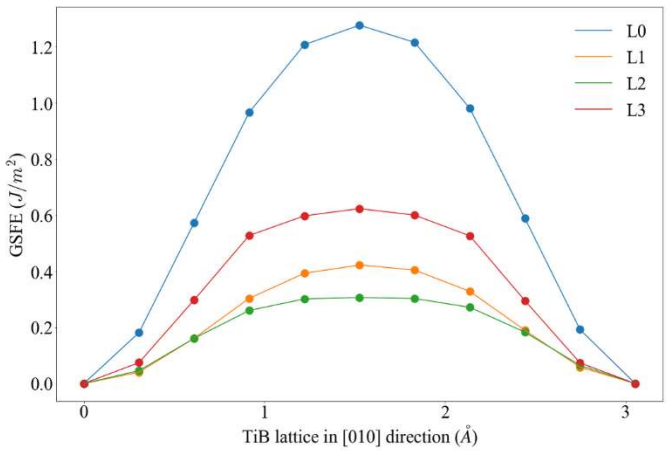

Fig. 6. Comparison of GSFE curves for levels L0~L3 of OR2 in the [010] direction.

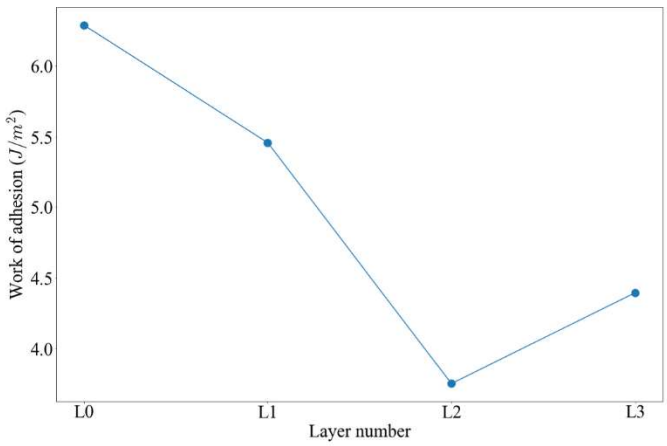

Fig. 7. The work of adhesion of levels L0~L3 of OR1.

the interface and subsequently affect the strength of the interface [47]. Such defects cannot be modeled by DFT since a large number of atoms is needed. Instead, MD simulations have been frequently used to study the MDN at interfaces [39,40,48].

To model the Ti/TiB interface at the nanoscale via MD, we utilized the second nearest-neighbor modified embedded atom method (2NN-

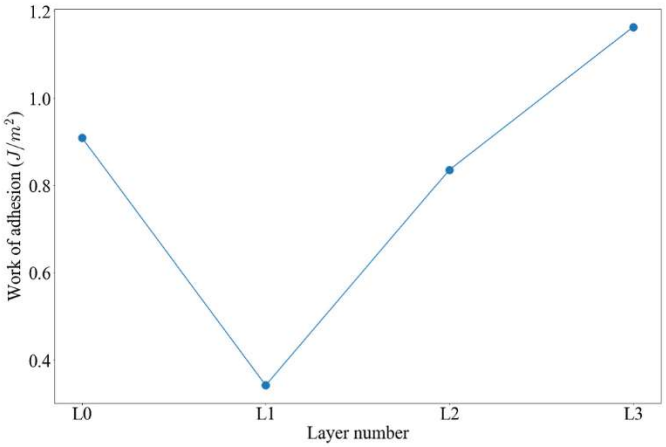

Fig. 8. The work of adhesion of levels L0~L3 of OR2.

MEAM) potentials developed by the authors for Ti–B interaction [49] and by Kim et al. for Ti [50]. We carefully chose the model's dimensions, so the stresses caused by the periodic boundaries were negligible. To achieve this, we determined multipliers c_1 and c_2 to enforce $c_1 \times l_1 \approx c_2 \times l_2$ where l_1 and l_2 are lattice constants of Ti and TiB in the desired periodic directions. The lattice constants are initially predicted by MD simulations. To study OR1, we generated a simulated system, which is periodic in the [010] (y) and [001] (z) directions and nonperiodic in the [100] (x) direction, as shown in Fig. 9(a). The predicted lattice constants of TiB and Ti are 3.054 Å and 2.945 Å in the [010] direction and 4.498 Å and 4.678 Å in the [001] direction, respectively. This causes 3.6% and 4.2% mismatches in the respective directions. In the [010] direction, we used 82 unit cells of TiB and 85 unit cells of Ti, i.e., $82 \times 3.054 \approx 85 \times 2.945 \approx 25\ nm$. Similarly, in the [001] direction, we used 74 unit cells of TiB and 71 unit cells of Ti so that this dimension is 33 *nm*. In addition, in the [100] direction, we used 10 unit cells for each material, and this choice is arbitrary and would not affect our results in this section. Overall, the generated system is $11\ nm \times 25\ nm \times 33\ nm$ and consists of more than 700,000 atoms.

In the OR2 case, the predicted lattice constants of TiB and Ti are 6.006 Å and 5.102 Å in the [100] direction and 3.054 Å and 2.945 Å in the [010] direction, respectively. This causes 15% and 3.6% mismatches in the respective directions. In the [100] direction, we used 79 unit cells of TiB and 93 unit cells of Ti, and in the [010] direction, we used 82 unit cells of TiB and 85 unit cells of Ti. In addition, in the [001] direction, we used 10 unit cells for each material. Overall, the size of the system is $47\ nm \times 25\ nm \times 9\ nm$. The system was periodic in the [100] (x) and [010] (y) directions and nonperiodic in the [001] (z) direction with more than 800,000 atoms, as shown in Fig. 12(a).

All the MD simulations in this research were performed using LAMMPS [51]. The simulations were initially started at $600\ K$ by assigning random velocities from the Maxwell-Boltzmann distribution

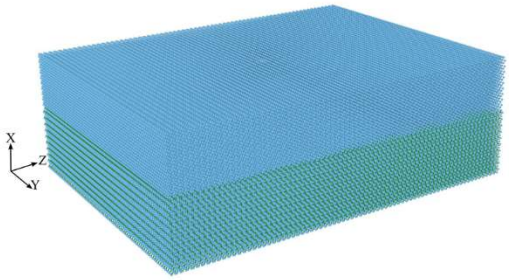

(a)

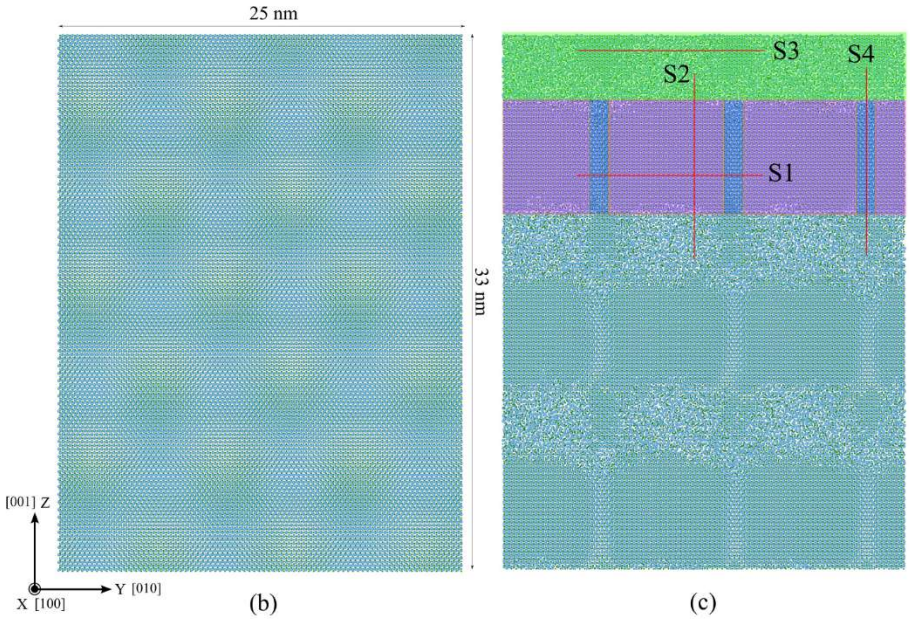

(b) (c)

Fig. 9. (a) The simulation setup of OR1, (b) the unrelaxed interface, and (c) the relaxed interface. The interface shown in (b) and (c) includes two layers of titanium above the interface and one unit cell of TiB below the interface.

and then quenched to 0.1 K during a controlled pressure – controlled temperature (NPT) ensemble at 1 bar through 10000 steps with a timestep of $10^{-15}s$ as is a conventional time step used in MD simulation [52,53]. This way, the atoms have enough time to relax at their equilibrium positions.

After the system's relaxation, we applied a shear deformation to the systems to observe the layers that started to slip. To apply the deformation, we fixed a layer with 6 Å thickness at the bottom to prevent the system's free body motion, and a displacement in the [010] direction was applied to a layer at the top with 6 Å thickness.

3.2. Misfit dislocation networks at OR1 and OR2

Fig. 9 shows the simulation model and the OR1 interface before and after relaxation. A pattern can be observed in the unrelaxed structure from the [100] view in Fig. 9(b) due to the different molecular structures of Ti and TiB. After relaxation, the atoms create a new pattern based on their preferred positions. In Fig. 9(c), three zones can be distinguished and colored purple, blue, and green. In addition, four cross-sections (S1, S2, S3, and S4) are marked. Fig. 10 shows cross-sections of S1 and S2 indicated in Fig. 9(c) (note that the coordinate system at the bottom left of each picture is for the view direction). Section S1 has a clean interface, especially in the purple zone (circled as region 3 in Fig. 10). In region 1 of the S1 section, an extra titanium atom has affected the bonding at the interface. It has caused a crystal distortion in region 2, corresponding to the blue zones in Fig. 9(c). The cross-section S2 in Fig. 10 shows that the middle part, which falls in the purple zone, has a coherent interface. In contrast, the end parts that belong to the green zone in Fig. 9(c) are largely disordered via interfacial diffusion. More details on cross-sections S3 and S4 and the induced defects in the titanium matrix are discussed in the supplementary material (Figures A.1 to A.3).

To observe the shear behavior of the interface via MD simulations, we applied a shear deformation with a rate of 0.1 Å/ps in the [010] direction to the top layers of the model. The system was maintained at NPT at 1 bar and 0.1 K. Fig. 11 shows the movement of the atoms during the shear deformation in the purple/blue zone. It is clear that the displacement occurs between layers T2 and T3 (indicated in Fig. 10). This is consistent with the findings of the GSFE studies discussed in Section 2.2, where the L2 level of the DFT model shown in Fig. 2(b), which corresponds to the interface between T2 and T3 of the MD model, had the weakest unstable stacking fault energy relative to the rest of the layers in its vicinity. Here, we studied the interfacial shear behavior only in the [010] direction because it is the main direction of load transfer from the Ti matrix to the TiB whiskers in Ti/TiB composites. The movement of the atoms in the green zone is provided in Figure A4 of the supplementary material.

Contrary to OR1, the OR2 interface did not show any discernible MDN. Fig. 12 shows the first and second layers of Ti atoms above the interface before and after the relaxation. The first Ti layer is affected the most by the existence of the interface (Fig. 12(c)). Due to the higher lattice mismatch in the [100] direction, several lines can be seen in the pictures caused by the Ti layer's strain to accommodate the mismatch. However, no noticeable effects can be observed in the second layer.

Fig. 13 shows the movement of the atoms at the OR2 interface when a shear deformation is applied. Obviously, the displacement occurs

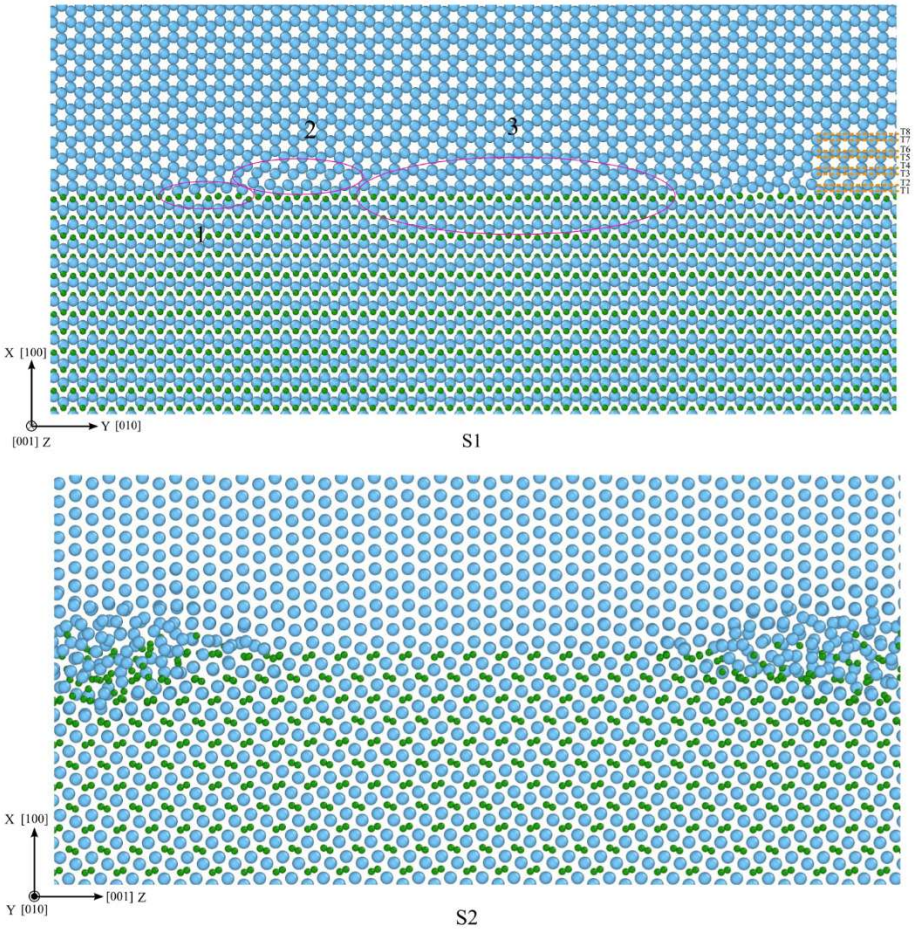

Fig. 10. Views of the cross-sections S1 and S2 are indicated in Fig. 9(c). The atomic displacements of the layers T1 ~ T8 indicated on the cross-section S1 are shown in the supplementary material (Figures A.2 and A.3).

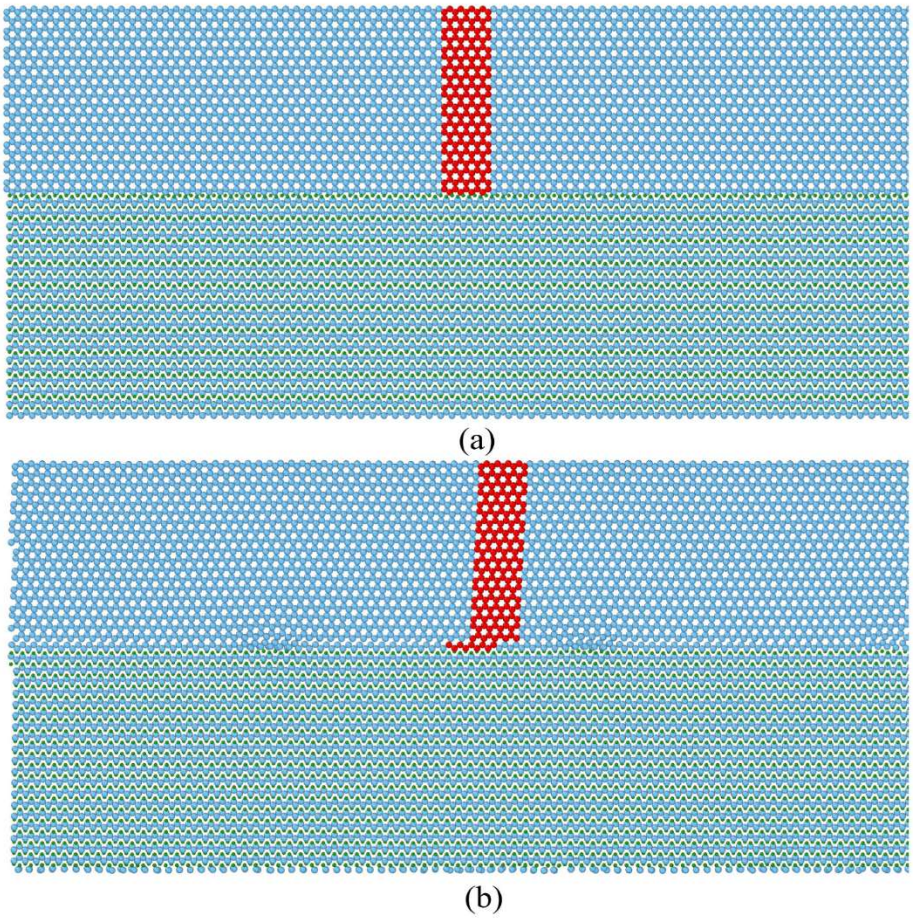

Fig. 11. Displacement due to the shear stress in the [010] direction at the purple/blue zone indicated in Fig. 9(c). The top picture shows the atoms before the displacement and the bottom picture shows the atoms after the displacement. A group of atoms is colored red to show where the slip occurs. (For interpretation of the references to color in this figure legend, the reader is referred to the Web version of this article.)

between the second and third Ti layers. This phenomenon is also consistent with the findings of the GSFE studies (Fig. 7) via DFT calculations, where the L2 level of Ti (indicated in Fig. 3) between the second and third Ti layers had the weakest unstable stacking fault energy relative to the rest of the layers in the vicinity.

4. Parametrizing CZM

4.1. Methodology for parametrizing CZM using MD

Cohesive zone models relate the traction at the interface to its separation. If traction exceeds the maximum tolerable value, the interface debonds, and a crack will initiate and propagate along the interface. The advantage of CZM over traditional fracture mechanics methods is that there is no need to embed an initial crack in the FEM mesh, and the CZM controls both the damage initiation and accumulation. Cohesive zone models have roots in the works of Dugdale [54], Barenblatt [55,56] and Hillerborg et al. [57]. Later, several formulations were proposed by Needleman [58–60], Tvergaard [61], Camacho and Ortiz [62], etc., for the traction-separation relationships. Gall et al. [63] conducted the first MD simulation on the interfaces and compared the results to CZM; since then, several researchers have used MD simulations to parametrize CZM for further applications in FEM analysis [64–68].

In this work, we used the bilinear model for the traction-separation curve, shown in Fig. 14, as implemented in the commercial software ABAQUS [69]. In Fig. 14, t_n^0 represents the maximum allowed stress in the normal direction, and t_s^0 and t_t^0 are the maximum allowed stress in the two shear directions, respectively. δ_n^0 is the normal separation between two interfaces at the maximum stress, and δ_n^f is the maximum normal separation when the interface debonds. The similar separations, δ_s^0, δ_t^0, δ_s^f, and δ_t^f, are also defined in the shear directions. For damage initiation, we use the quadratic stress criterion, which assumes that the damage initiates when:

$$\left\{\frac{t_n}{t_n^0}\right\}^2 + \left\{\frac{t_s}{t_s^0}\right\}^2 + \left\{\frac{t_t}{t_t^0}\right\}^2 = 1$$

where t_n, t_s, and t_t are the current tractions in the normal and two shear directions, respectively. In this work, we were only interested in the shear in the [010] direction, which is the main direction for load transfer from the Ti matrix to TiB whiskers. In addition, we assumed the same strength for other shear directions.

To parametrize the CZM, the interface's tensile strength and shear strength are needed to account for mode I and mode II failures. The simulation setup for the OR1 interface is shown in Fig. 15(a). The dimensions of the model are $18.2\,nm \times 12.1\,nm \times 13.6\,nm$ in the [100], [010], and [001] (x, y, and z) directions, respectively. The model is periodic in the y and z directions and nonperiodic in the x direction. A layer with 6 Å thickness at the bottom is fixed to prevent the system's free body motion, as illustrated in Fig. 16, and a displacement (tensile or shear) is applied to a layer at the top with 6 Å thickness. A region between ±15 Å of the interface is considered to measure the traction and separation (stress and displacement) during the simulations. The separation is measured as the difference between the average displacement

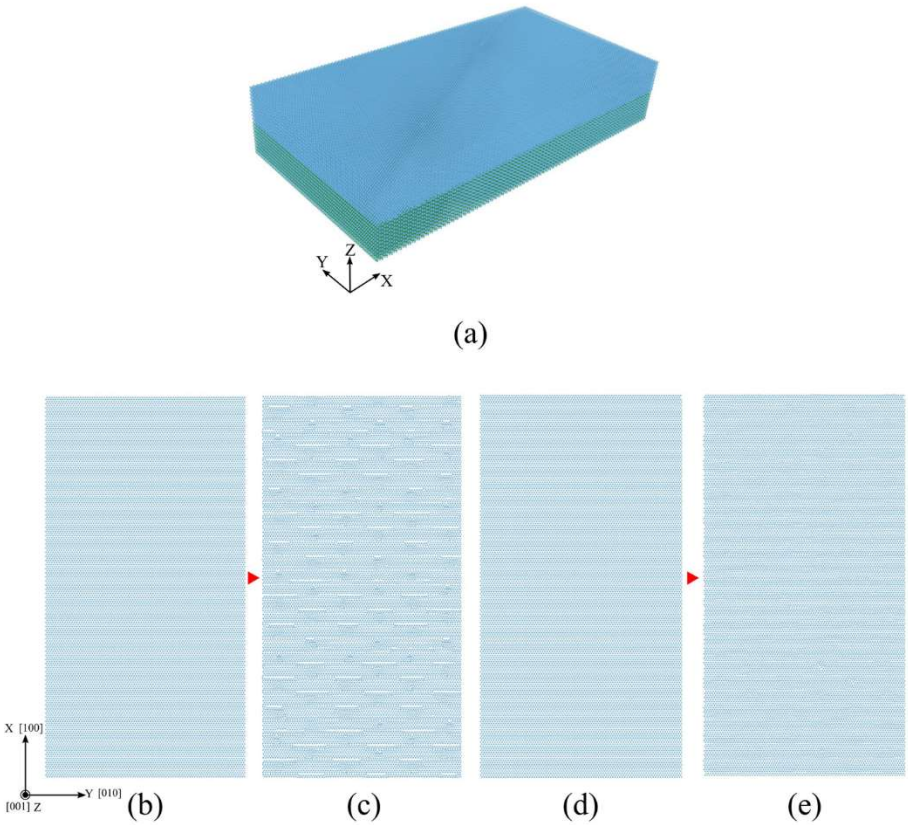

Fig. 12. (a) The simulation setup of OR2; (b) and (c) the first layer of titanium before and after relaxation; (d) and (e) the second layer of titanium before and after relaxation.

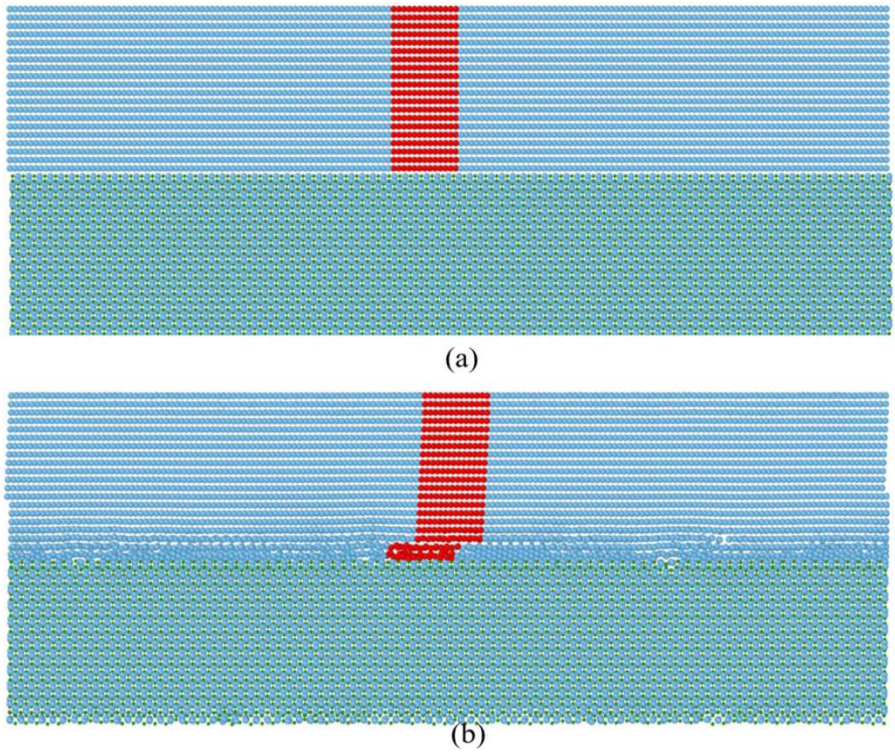

Fig. 13. Displacement due to the shear stress in the [010] direction. A group of atoms are colored red to show where the slip occurs. The top picture shows the atoms before the displacement and the bottom picture shows the atoms after the displacement. A group of atoms is colored red to show where the slip occurs. (For interpretation of the references to color in this figure legend, the reader is referred to the Web version of this article.)

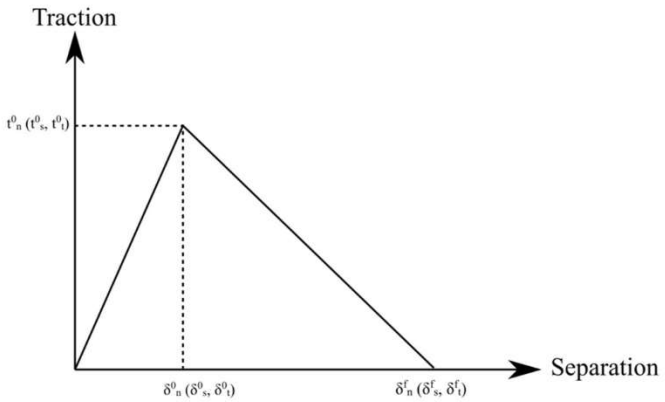

Fig. 14. The bilinear traction-separation diagram.

of the atoms within 15 Å above the interface and the average displacement of the atoms within 15 Å below the interface. The simulations are performed at a temperature of 300 K. At first, the whole model is relaxed at 300 K for 10000 steps with a timestep of 1 fs. Then, the displacement is applied to the top layer with a 5×10^8 $1/s$ strain rate through 250000 steps.

A similar simulation setup for OR2 is shown in Fig. 15(b). The dimensions of the model are $14nm \times 17.7nm \times 18.8nm$ in the [100], [010], and [001] (x, y, and z) directions, respectively. The model is periodic in the x and y directions and nonperiodic in the z direction. The other simulation parameters are the same as in the previous model.

4.2. Cohesive zone model parameters of OR1 and OR2 at 300 K

Fig. 17 shows the traction-separation (T-S) curve of OR1 at 300 K under tension. The blue curve is the result obtained from the MD simulation, and the red bilinear curve is the idealized model. The first red line is obtained using the slope of the curve at the initial stages of deformation, and it is extended up to the maximum tensile stress. Then, the second line is determined such that the area under the bilinear graph would be equal to the area under the actual curve obtained from the MD simulation. The resulted T-S parameters t^0_n, δ^0_n, and δ^f_n are 13.6 GPa, 1.13 Å, and 10.39 Å, respectively.

Fig. 18 shows the T-S curve of OR1 at 300 K under shearing in the [010] direction. As can be seen from the curve, after the first peak, the titanium layer starts to slip up to the point where the whole layer falls into the next potential well. This pattern repeats, with every peak being lower than the previous peak. Due to the limitations in the simulation

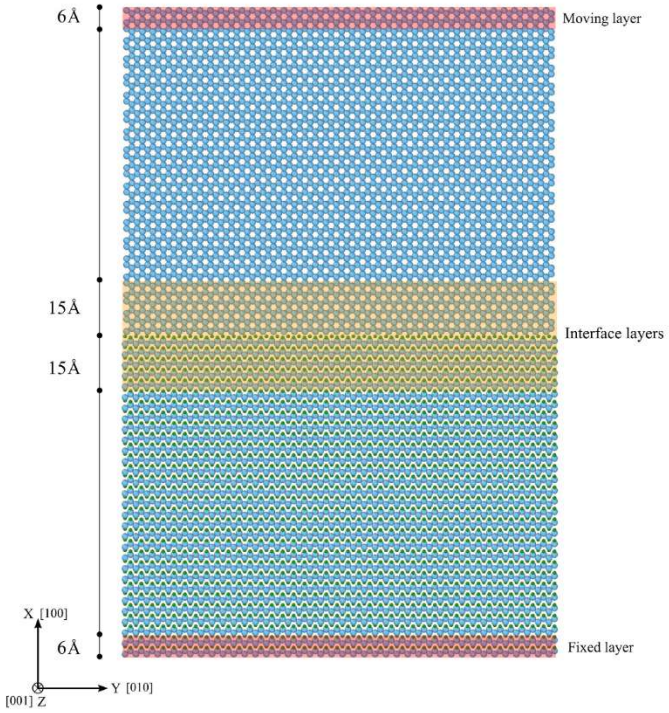

Fig. 16. Molecular dynamics model used for the simulations of OR1.

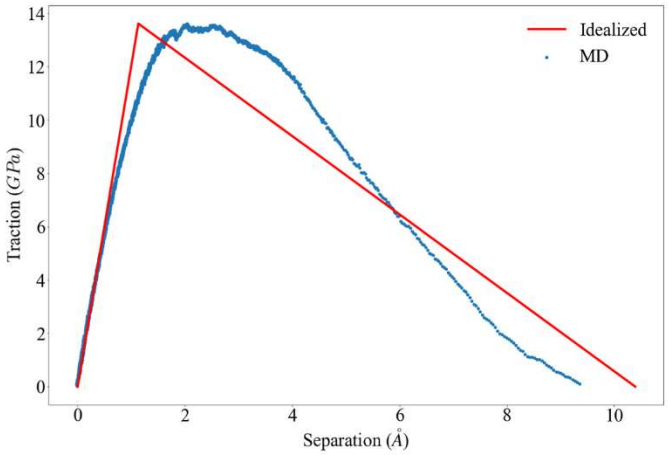

Fig. 17. Mode I traction-separation curve for OR1 at 300 K.

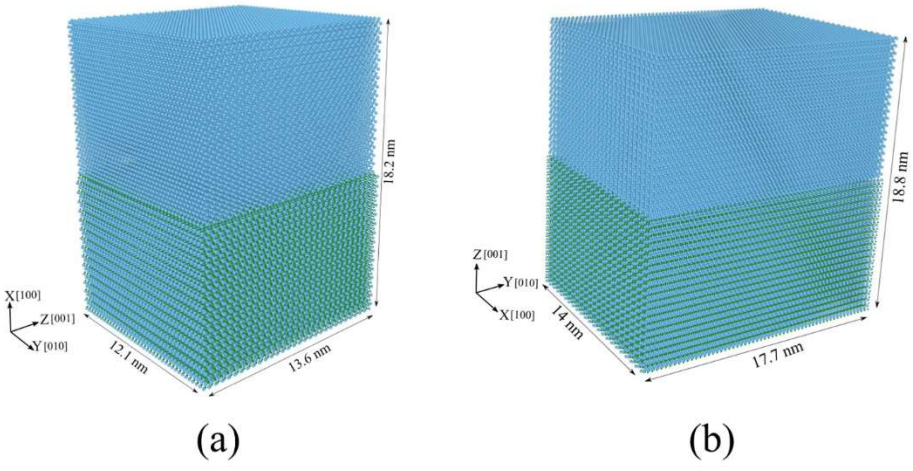

Fig. 15. The simulated models of (a) OR1 and (b) OR2 for tensile and shear tests.

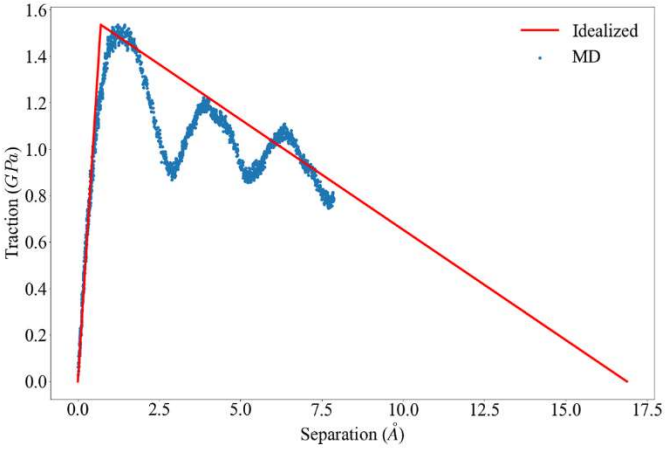

Fig. 18. Mode II traction-separation curve for OR1 at 300 K.

time, we let the simulation proceed up to the third peak. For the bilinear approximation of this behavior, we draw the first line based on the initial slope of the curve and extend the line up to the maximum shear stress. Then for the second line, we used the second peak of the curve and assumed a linear degradation of the shear strength. In the discussion section, we will discuss why such idealization of the second line does not impact the overall results of the simulation. From this curve, the values for t_s^0, δ_s^0, and δ_s^f are 1.53 GPa, 0.7 Å, and 16.58 Å, respectively.

The traction-separation curves of OR2 are provided in the supplementary material (Figures A5 and A.6). The CZM values of OR2 in mode I are 8.1 GPa, 0.92 Å, and 13.32 Å for t_n^0, δ_n^0, and δ_n^f, respectively; in mode II, they are 1.17 GPa, 0.28 Å, and 22.18 Å for t_s^0, δ_s^0, and δ_s^f, respectively. Overall, the results show that the OR1 interface has higher strength than the OR2 interface in both tensile and shear deformations.

5. FEM modeling the Ti/TiB interfaces with CZM

5.1. Modeling a single TiB whisker within the Ti matrix

To study the effects of the parametrized CZM on the mechanics of Ti–TiB via FEM simulations, we generated an RVE in which a single TiB whisker aligned in the applied uniaxial tension direction is placed in the Ti matrix.

In the first model (Fig. 19(a)), referred to as Model A, the TiB whisker is embedded completely inside the Ti matrix. One end of the model is fixed, and a displacement is applied to the other end of the model. In another scenario (Fig. 19(b)), the TiB whisker is brought to the front of the Ti matrix. Three different loading conditions were considered: (1) the displacement is applied to both the matrix and the whisker, (2) the displacement is applied only to the matrix, and (3) the displacement is applied only to the whisker. These models are referred to as Models B, C, and D, respectively.

Three different interface interactions were tested on these models: (1) the CZM for the OR1 interface (CZM1), (2) the CZM for the OR2 interface (CZM2), and (3) the tie constraint (i.e., the nodes of the matrix and the whisker at the interface are tied and move together during the FEM simulations). The commercial software ABAQUS/Explicit [69] was used for FEM simulations in our work. The size of all models is $5 \times 5 \times 20$ μm. The whisker is 16 μm long with a radius of 0.6 μm. The selected whisker length, radius, and cylindrical shape are similar to what was observed in the experiment [70]. Therefore, the failure stress of the whiskers in our FEM simulations would be valid.

Each model contains about 560,000 linear hexahedral elements of type C3D8R for both the matrix and the whisker. The seed size for meshing was chosen by starting from a large one and gradually reducing it while comparing the results (stress distribution, the overall elongation of the model before failure, etc.). We found that the results would converge when seed sizes were smaller than 0.1 μm. Therefore, we kept the seed size at 0.1 μm in all FEM models. In addition, during meshing, the software automatically decides the appropriate size of the elements based on the geometry of the region being meshed. For the Ti matrix, we used an elastic-perfectly plastic behavior with Young's modulus $E = 110GPa$, Poisson's ratio$\nu = 0.33$, yield strength $\sigma_y = 937MPa$, ultimate strength $\sigma_u = 1062MPa$, and elongation to failure of 16.5% obtained from Gaisin et al. [71]. For TiB, we used $E = 410.6GPa$ and $\nu = 0.166$, which we obtained using MD simulation at 300 K (room temperature). The failure stress of TiB whiskers was set to 8 GPa [70]. For the matrix, ductile damage was considered, with element removal after an element passes the maximum elongation. For TiB whiskers, brittle damage was assumed, with element removal if an element exceeds the assigned failure stress.

In FEM simulations via ABAQUS, contact between two surfaces can be modeled by providing interface properties or introducing a cohesive material between the surfaces. In the studies of Ti/TiB, we adopted the direct definition of contact and used the derived CZM parameters as the interface properties. We used a 'hard' pressure-overclosure option in ABAQUS to prevent the nodes of Ti and TiB from passing through each other if there was pressure at the interface. In addition, the interface was assumed to be frictionless. It is also common to use a very small viscosity term to maintain the stability of the numerical solution during the interface debonding [72], for which we used 10^{-5} [73].

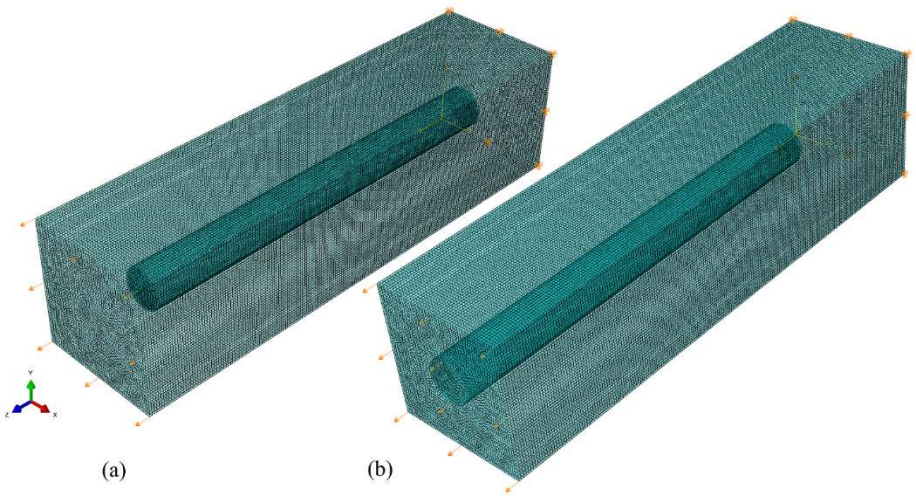

Fig. 19. FEM models used to test the CZM model.

5.2. Results

In all the models that we simulated, the interface tolerated the shear stress until either the matrix or the whisker failed. As an example, Fig. 20 shows the model where the whisker is completely inside the matrix and the displacement is applied directly to the matrix. The figure shows that the elements of the matrix on the left side of Fig. 20(a) (where the displacement has been applied) have failed. The whiskers in Fig. 20(b) and (c) show that no damage has occurred at the interfaces of CZM1 (b) and CZM2 (c). (The blue color indicates no damage, and red indicates complete debonding). The relevant figures for the rest of the models are provided in the supplementary material (Figures A7 to A.9).

Fig. 21 compares the stress-strain curves up to the failure points using the tie constraints, CZM1, and CZM2, in each of the four models described above. As a result of the strong interface, the curves almost completely fall on top of each other.

6. Discussion

In the previous sections, we studied the mechanical behavior of Ti/TiB interfaces under tensile and shear deformations at three different length scales with different assumptions. At the atomic scale using the DFT method, we assumed that there was no defect in any part of the model. Based on this assumption, our simulations showed that the interfaces between Ti and TiB (the L0 levels in Figs. 2 and 3) are stronger than the titanium layers close to the interfaces when subject to either tensile or shear deformation. This phenomenon was also observed for OR1 in another DFT study conducted by Zhang et al. [36]. In addition, OR2 is noticeably weaker than OR1 and has much lower adhesion than the titanium layers away from the interface. This weakness may be because of the formation process of the interface. During the production of α-Ti/TiB composites, if the temperature is kept below 910 °C, titanium remains in the α phase, and OR1 is the main interface observed [22]. If the temperature exceeds 910 °C, there exists an α→β phase transformation in Ti. In the β phase, another orientation relationship is observed in experimental works [22]: $(001)_{TiB} \parallel (110)_{\beta-Ti}$ with $[010]_{TiB} \parallel [\bar{1}11]_{\beta-Ti}$. After the temperature drops and titanium changes its phase back to α, the mentioned interface turns into OR2. This back-and-forth phase change limits the possible options of forming an interface between Ti and TiB, affecting the strength of the final OR2. More about the experimental observations of the orientation relationships of Ti/TiB can be found in the work of Ozerov et al. [22] and the references therein.

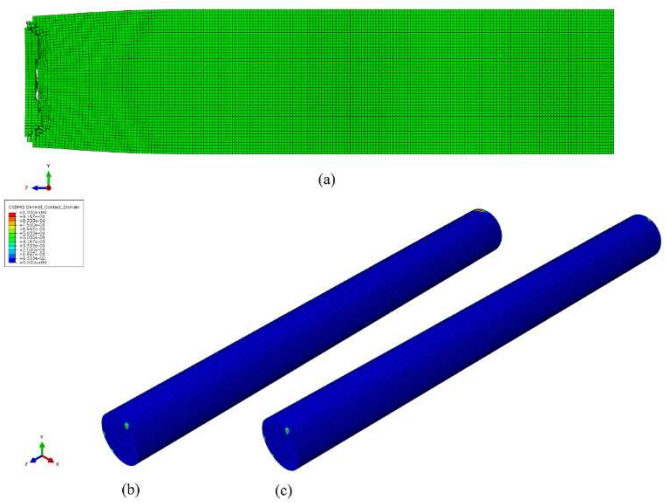

Fig. 20. Results of the first simulation set: the first FEM model with three different interface interactions.

The 2NN-MEAM potential function used in this study was developed in our previous work [49] and has been validated by comparing materials properties obtained from MD simulations with the experimental measurements. Using MD simulations in this study, we constructed a larger model of the interface and conducted the simulations at 300 K. It is assumed that the Ti and TiB layers are defect-free, while the interface has defects due to the misfit dislocation network. The misfit dislocation networks were commonly observed in the experiments [46] if the lattice constants of two materials do not match each other at the interface. The shear deformation tests for these models showed that the slip happens not exactly at the interface but at the levels in Ti close to the interface. It was also observed that the layers where the slip started in both the OR1 and OR2 models coincided with the weakest levels obtained from DFT simulations, although the different assumptions were applied at different length scales.

When reaching the largest length scale at the continuum level, the definition of "interface" becomes slightly different. All the layers in the vicinity of the L0 level of Ti/TiB could be called interface regions when looking from the perspective of the whole composite. To parametrize the CZM, we took a region within ±15 Å of the L0 level as the interface region and showed that the slip happens in the interface region when the shear stress reaches 1.53 and 1.17 GPa for OR1 and OR2, respectively.

Using these values in the finite element model with actual failure strengths of Ti and TiB, we observed that the interface region could transfer the load between Ti and TiB without losing its load-bearing capacity until either Ti or TiB failed. This could also be shown analytically by considering the failure shear stress of the titanium alloy used in this work, $\tau_y = \frac{\sigma_y}{\sqrt{3}} = \frac{0.973}{\sqrt{3}} \cong 0.562\ GPa$, which is lower than the failure shear stress of both OR1 and OR2 (1.53 and 1.17 GPa). Hence, we conclude that in α-Ti/TiB composites, as long as OR1 and OR2 are the dominant interfaces, the failure of the composite is not initiated by interfacial debonding. This phenomenon has also been observed in the experimental tensile tests, indicating that Ti/TiB composite at room temperature did not have any signs of debonding between the whisker and the matrix [71,74,75]. In addition, the interface may have debonded only after the whisker fracture [76]. On the other hand, in their work [70], Boehlert et al. assumed that the interface should be intact during the tensile failure to measure the failure stress of TiB whiskers, which to date is the only experimentally reported failure stress for TiB.

It is worth mentioning two points here related to the CZM model. The first is that the bilinear model could be a good approximation for the tensile T-S curve, but it does not represent the oscillatory behavior of the shear T-S curve in Fig. 18 and A6 well. This is not an issue in our simulations since the traction at the interface never passes the peak point and always remains in the first idealized line. The second point is that the length scales of T-S curves are in the nm range, which is typical for metal/ceramic interfaces [77], but the whisker model is in the μm length scale. Therefore, such FEM modeling needs a very fine mesh to perform an accurate simulation. Also, to account for the brittle damage for TiB in ABAQUS, one needs to perform a dynamic analysis that requires considering the density of each material. Due to the extremely low mass of each element, a large number of time steps are required to perform an accurate simulation, even with a mass scaling factor of 10^6. This is why we limited our FEM model to a single whisker with about 500,000 elements. To ensure that the selected mass scaling does not affect the results, we also tried running one of the simulations with mass scaling of 10^5, giving the same results but with a much longer run time. Our final comparison in Fig. 21 shows that modeling Ti/TiB composites with the tie constraint yields the same results as modeling with CZM but was five times faster in computation time.

7. Conclusions

This work investigates two experimentally verified interfaces between α-Ti and TiB through different numerical methods at different

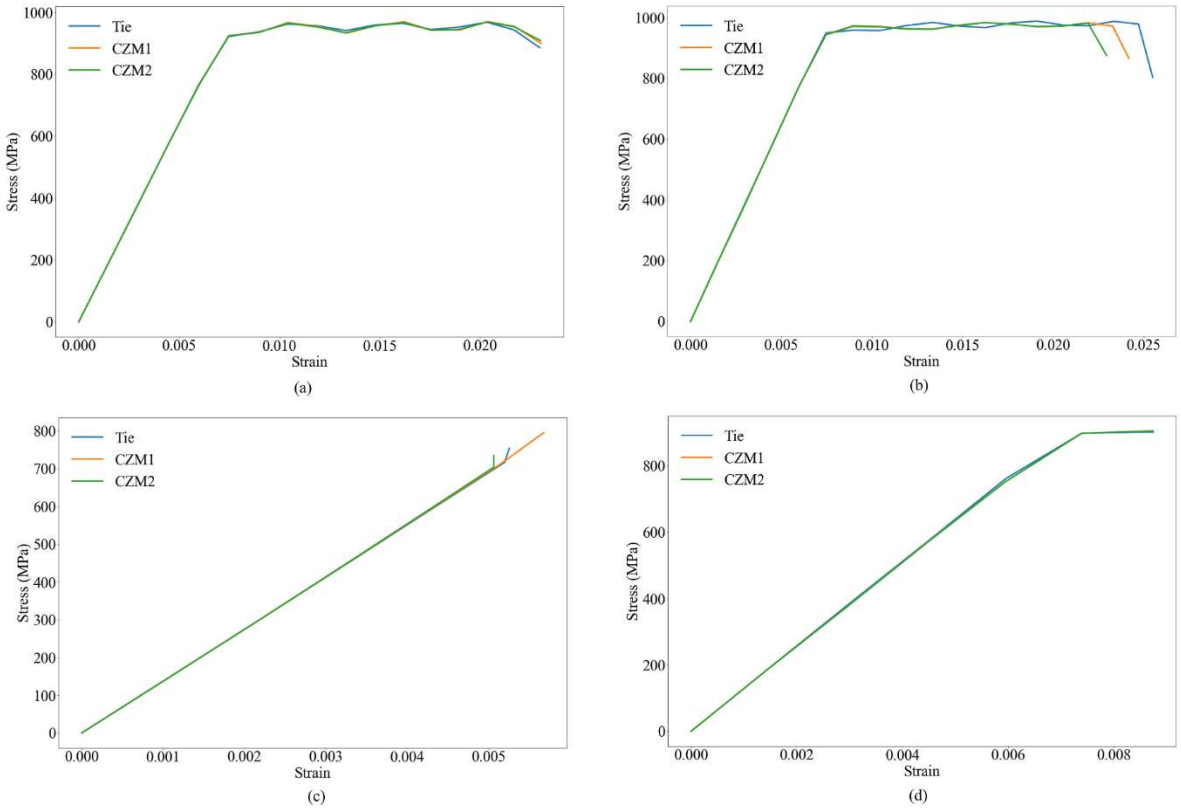

Fig. 21. Stress-strain curves of the four simulation sets.

length scales. Using DFT, we showed that the interface level is stronger in both the OR1 and OR2 interfaces than in any layers within Ti. We also showed that OR1 is stronger than the OR2 interface formed from the back-and-forth phase transformation during the production of Ti/TiB composites. We assessed the effects of misfit dislocation networks on the behavior of the interfaces during shear deformation using MD simulations. The obtained results were consistent with the results from DFT, which predicted that the gliding planes during shear deformation were in the Ti matrix and close to the interface. We parametrized a CZM model and performed FEM simulations using the developed model at room temperature. Our results showed that both OR1 and OR2 interfaces could transfer shear load from Ti to TiB without failure, and this was supported by experimental results. It is suggested that Ti/TiB composites can be modeled in FEM by assuming the tie constraints between the nodes of the matrix and the whisker at their interface and can save considerable simulation time. Future works could be focused on measuring the failure strength of TiB whiskers using the results of tension tests by assuming a perfect cohesion between Ti and TiB.

CRediT authorship contribution statement

Siamak Attarian: Conceptualization, Methodology, Writing – original draft. **Shaoping Xiao:** Supervision, Writing – review & editing.

Declaration of competing interest

The authors declare that they have no known competing financial interests or personal relationships that might influence the work reported in this paper.

Acknowledgment

The authors gratefully acknowledge the support from the National Science Foundation (#2104383) and the US Department of Education (ED#P116S210005).

Appendix A. Supplementary data

Supplementary data to this article can be found online at https://doi.org/10.1016/j.ceramint.2022.07.259.

References

[1] P.E. Deierling, O.I. Zhupanska, C.L. Pasiliao, Spatial tailoring of a metal-ceramic composite panel subjected to high-speed flow, J. Aero. Eng. 34 (2021), 04020093, https://doi.org/10.1061/(asce)as.1943-5525.0001215.

[2] H. Attar, S. Ehtemam-Haghighi, N. Soro, D. Kent, M.S. Dargusch, Additive manufacturing of low-cost porous titanium-based composites for biomedical applications: advantages, challenges and opinion for future development, J. Alloys Compd. 827 (2020), 154263, https://doi.org/10.1016/j.jallcom.2020.154263.

[3] B. Song, C. Kenel, D.C. Dunand, 3D ink-extrusion printing and sintering of Ti, Ti-TiB and Ti-TiC microlattices, Addit. Manuf. 35 (2020), 101412, https://doi.org/10.1016/j.addma.2020.101412.

[4] M. Ozerov, N. Stepanov, A. Kolesnikov, V. Sokolovsky, S. Zherebtsov, Brittle-to-ductile transition in a Ti–TiB metal-matrix composite, Mater. Lett. 187 (2017) 28–31, https://doi.org/10.1016/j.matlet.2016.10.060.

[5] P. Klimczyk, E. Benko, K. Lawniczak-Jablonska, E. Piskorska, M. Heinonen, A. Ormaniec, W. Gorczynska-Zawislan, V.S. Urbanovich, Cubic boron nitride - Ti/TiN composites: hardness and phase equilibrium as function of temperature, J. Alloys Compd. 382 (2004) 195–205, https://doi.org/10.1016/j.jallcom.2004.04.140.

[6] A. Shamsipur, S.F. Kashani-Bozorg, A. Zarei-Hanzaki, The effects of friction-stir process parameters on the fabrication of Ti/SiC nano-composite surface layer, Surf. Coating. Technol. 206 (2011) 1372–1381, https://doi.org/10.1016/j.surfcoat.2011.08.065.

[7] X.N. Mu, H.M. Zhang, H.N. Cai, Q.B. Fan, Z.H. Zhang, Y. Wu, Z.J. Fu, D.H. Yu, Microstructure evolution and superior tensile properties of low content graphene nanoplatelets reinforced pure Ti matrix composites, Mater. Sci. Eng. 687 (2017) 164–174, https://doi.org/10.1016/j.msea.2017.01.072.

[8] C. Wu, Z. Wang, Q. Li, G. Shi, M. Liu, Y. Li, Mechanical properties and microstructure evolution of Ti/Al 2O3 cermet composite with CeO2 addition, J. Alloys Compd. 617 (2014) 729–733, https://doi.org/10.1016/j.jallcom.2014.08.007.

[9] M. Das, K. Bhattacharya, S.A. Dittrick, C. Mandal, V.K. Balla, T.S. Sampath Kumar, A. Bandyopadhyay, I. Manna, In situ synthesized TiB-TiN reinforced Ti6Al4V alloy composite coatings: microstructure, tribological and in-vitro biocompatibility,

J. Mech. Behav. Biomed. Mater. 29 (2014) 259–271, https://doi.org/10.1016/j.jmbbm.2013.09.006.
[10] L. Huang, Q. An, L. Geng, S. Wang, S. Jiang, X. Cui, R. Zhang, F. Sun, Y. Jiao, X. Chen, C. Wang, Multiscale Architecture and superior high-temperature performance of discontinuously, Adv. Mater. 33 (2021), 2000688, https://doi.org/10.1002/adma.202000688.
[11] K. Morsi, V.V. Patel, S. Naraghi, J.E. Garay, Processing of titanium-titanium boride dual matrix composites, J. Mater. Process. Technol. 196 (2008) 236–242, https://doi.org/10.1016/j.jmatprotec.2007.05.047.
[12] T. Saito, The automotive application of discontinuously reinforced TiB-Ti composites, JOM (J. Occup. Med.) 56 (2004) 33–36, https://doi.org/10.1007/s11837-004-0125-3.
[13] H. Attar, L. Löber, A. Funk, M. Calin, L.C. Zhang, K.G. Prashanth, S. Scudino, Y. S. Zhang, J. Eckert, Mechanical behavior of porous commercially pure Ti and Ti-TiB composite materials manufactured by selective laser melting, Mater. Sci. Eng. 625 (2015) 350–356, https://doi.org/10.1016/j.msea.2014.12.036.
[14] S. Gorsse, J.P. Chaminade, Y. Le Petitcorps, In situ preparation of titanium base composites reinforced by TiB single crystals using a powder metallurgy technique, Compos. Part A Appl. Sci. Manuf. 29 (1998) 1229–1234, https://doi.org/10.1016/S1359-835X(98)00080-3.
[15] H. Feng, Y. Zhou, D. Jia, Q. Meng, J. Rao, Growth mechanism of in situ TiB whiskers in spark plasma sintered TiB/Ti metal matrix composites, Cryst. Growth Des. 6 (2006) 1626–1630, https://doi.org/10.1021/cg050443k.
[16] H. Feng, D. Jia, Y. Zhou, Spark plasma sintering reaction synthesized TiB reinforced titanium matrix composites, Compos. Part A Appl. Sci. Manuf. 36 (2005) 558–563, https://doi.org/10.1016/j.compositesa.2004.09.003.
[17] C. Cai, C. Radoslaw, J. Zhang, Q. Yan, S. Wen, B. Song, Y. Shi, In-situ preparation and formation of TiB/Ti-6Al-4V nanocomposite via laser additive manufacturing: microstructure evolution and tribological behavior, Powder Technol. 342 (2019) 73–84, https://doi.org/10.1016/j.powtec.2018.09.088.
[18] B.J. Kooi, Y.T. Pei, J.T.M. De Hosson, The evolution of microstructure in a laser clad TiB-Ti composite coating, Acta Mater. 51 (2003) 831–845, https://doi.org/10.1016/S1359-6454(02)00475-5.
[19] K. Zhang, X. Tian, M. Bermingham, J. Rao, Q. Jia, Y. Zhu, X. Wu, S. Cao, A. Huang, Effects of boron addition on microstructures and mechanical properties of Ti-6Al-4V manufactured by direct laser deposition, Mater. Des. 184 (2019), https://doi.org/10.1016/j.matdes.2019.108191.
[20] Y.F. Yang, M. Yan, S.D. Luo, G.B. Schaffer, M. Qian, Modification of the a -Ti laths to near equiaxed a -Ti grains in as-sintered titanium and titanium alloys by a small addition of boron, J. Alloys Compd. 579 (2013) 553–557, https://doi.org/10.1016/j.jallcom.2013.07.097.
[21] X. Guo, L. Wang, M. Wang, J. Qin, D. Zhang, W. Lu, Effects of degree of deformation on the microstructure, mechanical properties and texture of hybrid-reinforced titanium matrix composites, Acta Mater. 60 (2012) 2656–2667, https://doi.org/10.1016/j.actamat.2012.01.032.
[22] M. Ozerov, M. Klimova, A. Vyazmin, N. Stepanov, S. Zherebtsov, Orientation relationship in a Ti/TiB metal-matrix composite, Mater. Lett. 186 (2017) 168–170, https://doi.org/10.1016/j.matlet.2016.09.124.
[23] P. Nandwana, J.Y. Hwang, M.Y. Koo, J. Tiley, S.H. Hong, R. Banerjee, Formation of equiaxed alpha and titanium nitride precipitates in spark plasma sintered TiB/Ti-6Al-4V composites, Mater. Lett. 83 (2012) 202–205, https://doi.org/10.1016/j.matlet.2012.05.132.
[24] L. Sun, Y. Gao, B. Xiao, Y. Li, G. Wang, Anisotropic elastic and thermal properties of titanium borides by first-principles calculations, J. Alloys Compd. 579 (2013) 457–467, https://doi.org/10.1016/j.jallcom.2013.06.119.
[25] K.B. Panda, K.S.R. Chandran, First principles determination of elastic constants and chemical bonding of titanium boride (TiB) on the basis of density functional theory, Acta Mater. 54 (2006) 1641–1657, https://doi.org/10.1016/j.actamat.2005.12.003.
[26] R.R. Atri, K.S. Ravichandran, S.K. Jha, Elastic properties of in-situ processed Ti-TiB composites measured by impulse excitation of vibration, Mater. Sci. Eng. 271 (1999) 150–159, https://doi.org/10.1016/s0921-5093(99)00198-7.
[27] G. Constantinides, K.S. Ravi Chandran, F.J. Ulm, K.J. Van Vliet, Grid indentation analysis of composite microstructure and mechanics: principles and validation, Mater. Sci. Eng. 430 (2006) 189–202, https://doi.org/10.1016/j.msea.2006.05.125.
[28] H. Singh, M. Hayat, H. Zhang, R. Das, P. Cao, Effect of TiB2 content on microstructure and properties of in situ Ti–TiB composites, Int. J. Miner. Metall. Mater. 26 (2019) 915–924, https://doi.org/10.1007/s12613-019-1797-6.
[29] H. Singh, M. Hayat, Z. He, V.K. Peterson, R. Das, P. Cao, In situ neutron diffraction observations of Ti-TiB composites, Compos. Part A Appl. Sci. Manuf. 124 (2019) 2–6, https://doi.org/10.1016/j.compositesa.2019.105501.
[30] F. Ma, P. Liu, W. Li, X. Liu, X. Chen, K. Zhang, D. Pan, W. Lu, The mechanical behavior dependence on the TiB whisker realignment during hot-working in titanium matrix composites, Sci. Rep. 6 (2016) 1–9, https://doi.org/10.1038/srep36126.
[31] L.R. Dharani, M.N. Rahaman, S.H. Wang, Interfacial shear stress in SiC fibre-reinforced cordierite, J. Mater. Sci. 26 (1991) 655–660, https://doi.org/10.1007/BF00588300.
[32] N. Graupner, J. Rößler, G. Ziegmann, J. Müssig, Fibre/matrix adhesion of cellulose fibres in PLA, PP and MAPP: a critical review of pull-out test, microbond test and single fibre fragmentation test results, Compos. Part A Appl. Sci. Manuf. 63 (2014) 133–148, https://doi.org/10.1016/j.compositesa.2014.04.011.
[33] C. Shih, Y. Katoh, K.J. Leonard, H. Bei, E. Lara-Curzio, Determination of interfacial mechanical properties of ceramic composites by the compression of micro-pillar test specimens, J. Mater. Sci. 48 (2013) 5219–5224, https://doi.org/10.1007/s10853-013-7311-z.
[34] P. Nandwana, N. Gupta, S.G. Srinivasan, R. Banerjee, A first principles study of commonly observed planar defects in Ti/TiB system, Comput. Mater. Sci. 150 (2018) 197–201, https://doi.org/10.1016/j.commatsci.2018.04.006.
[35] R. Fan, Q. Zheng, Y. Liu, T. Fan, Insights into the interfacial bonding strength of TiB/Ti: a first principles study, J. Appl. Phys. 126 (2019), https://doi.org/10.1063/1.5109647.
[36] T. Zhang, N. Zhao, C. Shi, C. He, E. Liu, Regulation of the interface binding and mechanical properties of TiB/Ti via doping-induced chemical and structural effects, Comput. Mater. Sci. 174 (2020), 109506, https://doi.org/10.1016/j.commatsci.2019.109506.
[37] Q. An, L. Huang, Q. Qian, Y. Jiang, S. Wang, R. Zhang, L. Geng, L. Wang, Insights into in-situ TiB/dual-phase Ti alloy interface and its high load-bearing capacity, J. Mater. Sci. Technol. 119 (2022) 156–166, https://doi.org/10.1016/j.jmst.2021.12.035.
[38] A.S. Mohammad Miraz, S. Sun, S. Shao, W.J. Meng, B.R. Ramachandran, C. D. Wick, Computational study of metal/ceramic interfacial adhesion and barriers to shear displacement, Comput. Mater. Sci. 168 (2019) 104–115, https://doi.org/10.1016/j.commatsci.2019.06.006.
[39] X.Q. Fu, L.H. Liang, Y.G. Wei, Atomistic simulation study on the shear behavior of Ag/MgO interface, Comput. Mater. Sci. 155 (2018) 116–128, https://doi.org/10.1016/j.commatsci.2018.08.047.
[40] X. Zhang, B. Zhang, Y. Mu, S. Shao, C.D. Wick, B.R. Ramachandran, W.J. Meng, Mechanical failure of metal/ceramic interfacial regions under shear loading, Acta Mater. 138 (2017) 224–236, https://doi.org/10.1016/j.actamat.2017.07.053.
[41] X. Wu, T. Sun, R. Wang, L. Liu, Q. Liu, Energy investigations on the adhesive properties of Al/TiC interfaces: first-principles study, Phys. B Condens. Matter 449 (2014) 269–273, https://doi.org/10.1016/j.physb.2014.05.037.
[42] P. Giannozzi, S. Baroni, N. Bonini, M. Calandra, R. Car, C. Cavazzoni, D. Ceresoli, G.L. Chiarotti, M. Cococcioni, I. Dabo, A. Dal Corso, S. De Gironcoli, S. Fabris, G. Fratesi, R. Gebauer, U. Gerstmann, C. Gougoussis, A. Kokalj, M. Lazzeri, L. Martin-Samos, N. Marzari, F. Mauri, R. Mazzarello, S. Paolini, A. Pasquarello, L. Paulatto, C. Sbraccia, S. Scandolo, G. Sclauzero, A.P. Seitsonen, A. Smogunov, P. Umari, R.M. Wentzcovitch, Quantum ESPRESSO: a modular and open-source software project for quantum simulations of materials, J. Phys. Condens. Matter 21 (2009), https://doi.org/10.1088/0953-8984/21/39/395502.
[43] P.E. Blöchl, Projector augmented-wave method, Phys. Rev. B 50 (1994) 17953–17979, https://doi.org/10.1103/PhysRevB.50.17953.
[44] J.P. Perdew, K. Burke, M. Ernzerhof, Generalized gradient approximation made simple, Phys. Rev. Lett. (1996) 3865–3868.
[45] P. Kwasniak, H. Garbacz, K.J. Kurzydlowski, Solid solution strengthening of hexagonal titanium alloys: restoring forces and stacking faults calculated from first principles, Acta Mater. 102 (2016) 304–314, https://doi.org/10.1016/j.actamat.2015.09.041.
[46] M. Jw, A.E. Blakeslee, Defects in epitaxial multilayers, I. Misfit dislocations J, Lect. Notes Comput. Sci. 27 (1974) 118–125.
[47] M.W. Finnis, The theory of metal–ceramic interfaces M, J. Phys. Condens. Matter 8 (1996) 5811–5836.
[48] T. Liang, M. Ashton, K. Choudhary, D. Zhang, A.F. Fonseca, B.C. Revard, R. G. Hennig, S.R. Phillpot, S.B. Sinnott, Properties of Ti/TiC interfaces from molecular dynamics simulations, J. Phys. Chem. C 120 (2016) 12530–12538, https://doi.org/10.1021/acs.jpcc.6b02763.
[49] S. Attarian, S. Xiao, Development of a 2NN-MEAM potential for TiB system and studies of the temperature dependence of the nanohardness of TiB2, Comput. Mater. Sci. 201 (2022), https://doi.org/10.1016/j.commatsci.2021.110875.
[50] Y. Kim, B. Lee, M.I. Baskes, Modified embedded-atom method interatomic potentials for Ti and Zr (2006), https://doi.org/10.1103/PhysRevB.74.014101.
[51] A.P. Thompson, H.M. Aktulga, R. Berger, D.S. Bolintineanu, W.M. Brown, P. S. Crozier, P.J. in 't Veld, A. Kohlmeyer, S.G. Moore, T.D. Nguyen, R. Shan, M. J. Stevens, J. Tranchida, C. Trott, S.J. Plimpton, Lammps - a flexible simulation tool for particle-based materials modeling at the atomic, meso, and continuum scales, Comput. Phys. Commun. 271 (2022), 108171, https://doi.org/10.1016/j.cpc.2021.108171.
[52] Y. Li, A. Goyal, A. Chernatynskiy, J.S. Jayashankar, M.C. Kautzky, S.B. Sinnott, S. R. Phillpot, Nanoindentation of gold and gold alloys by molecular dynamics simulation, Mater. Sci. Eng. 651 (2016) 346–357, https://doi.org/10.1016/j.msea.2015.10.081.
[53] T.C. O'Connor, J. Andzelm, M.O. Robbins, AIREBO-M: a reactive model for hydrocarbons at extreme pressures, J. Chem. Phys. 142 (2015), https://doi.org/10.1063/1.4905549.
[54] D.S. Dugdale, Yielding of steel sheets containing slits, J. Mech. Phys. Solid. 8 (1960) 100–104, https://doi.org/10.12989/cac.2015.15.5.735.
[55] G.I. Barenblatt, The formation of equilibrium cracks during brittle fracture. General ideas and hypotheses. Axially-symmetric cracks, J. Appl. Math. Mech. 23 (1959) 622–636, https://doi.org/10.1016/0021-8928(59)90157-1.
[56] G.I. Barenblatt, Barenblatt, Adv. Appl. Mech. 7 (1962) 55–129.
[57] A. Hillerborg, M. Modéer, P.E. Petersson, Analysis of crack formation and crack growth in concrete by means of fracture mechanics and finite elements, Cement Concr. Res. 6 (1976) 773–781, https://doi.org/10.1016/0008-8846(76)90007-7.
[58] A. Needleman, Continuum model for void nucleation by inclusion debonding, Am. Soc. Mech. Eng. 54 (1987) 525–531.
[59] A. Needleman, An analysis of decohesion along an imperfect interface, Int. J. Fract. 42 (1990) 21–40, https://doi.org/10.1007/BF00018611.

[60] A. Needleman, Micromechanical modelling of interfacial decohesion, Ultramicroscopy 40 (1992) 203–214, https://doi.org/10.1016/0304-3991(92)90117-3.
[61] V. Tvergaard, Fibre debonding and breakage in a whisker-reinforced metal, Mater. Sci. Eng. 190 (1995) 215–222, https://doi.org/10.1016/0921-5093(95)80005-0.
[62] G.T. Camacho, M. Ortiz, Computational modelling of impact damage in brittle materials, Int. J. Solid Struct. 33 (1996) 2899–2938, https://doi.org/10.1016/0020-7683(95)00255-3.
[63] K. Gall, M.F. Horstemeyer, M. Van Schilfgaarde, M.I. Baskes, Atomistic simulations on the tensile debonding of an aluminum-silicon interface, J. Mech. Phys. Solid. 48 (2000) 2183–2212, https://doi.org/10.1016/S0022-5096(99)00086-1.
[64] E.H. Glaessgen, E. Saether, D.R. Phillips, V. Yamakov, Multiscale modeling of grain-boundary fracture: cohesive zone models parameterized from atomistic simulations, in: Collect. Tech. Pap. - AIAA/ASME/ASCE/AHS/ASC Struct. Struct. Dyn. Mater. Conf., vol. 2, 2006, pp. 959–970, https://doi.org/10.2514/6.2006-1674.
[65] M. Lu, F. Wang, X. Zeng, W. Chen, J. Zhang, Cohesive zone modeling for crack propagation in polycrystalline NiTi alloys using molecular dynamics, Theor. Appl. Fract. Mech. 105 (2020), 102402, https://doi.org/10.1016/j.tafmec.2019.102402.
[66] H. Pen, J. Guo, Z. Cao, X. Wang, Z. Wang, Finite element simulation of the micromachining of nanosized-silicon-carbide-particle reinforced composite materials based on the cohesive zone model, Nami Jishu Yu Jingmi Gongcheng/Nanotechnology Precis. Eng. 1 (2018) 242–247, https://doi.org/10.1016/j.npe.2018.12.003.
[67] W.G. Jiang, Y. Wu, Q.H. Qin, D.S. Li, X.B. Liu, M.F. Fu, A molecular dynamics based cohesive zone model for predicting interfacial properties between graphene coating and aluminum, Comput. Mater. Sci. 151 (2018) 117–123, https://doi.org/10.1016/j.commatsci.2018.05.008.
[68] M.G. Elkhateeb, Y.C. Shin, Molecular dynamics-based cohesive zone representation of Ti6Al4V/TiC composite interface, Mater. Des. 155 (2018) 161–169, https://doi.org/10.1016/j.matdes.2018.05.054.
[69] M. Smith, ABAQUS/Standard User's Manual, 2009, Version 6.9.
[70] C.J. Boehlert, S. Tamirisakandala, W.A. Curtin, D.B. Miracle, Assessment of in situ TiB whisker tensile strength and optimization of TiB-reinforced titanium alloy design, Scripta Mater. 61 (2009) 245–248, https://doi.org/10.1016/j.scriptamat.2009.03.054.
[71] R.A. Gaisin, V.M. Imayev, R.M. Imayev, Effect of hot forging on microstructure and mechanical properties of near α titanium alloy/TiB composites produced by casting, J. Alloys Compd. 723 (2017) 385–394, https://doi.org/10.1016/j.jallcom.2017.06.287.
[72] Y.F. Gao, A.F. Bower, A simple technique for avoiding convergence problems in finite element simulations of crack nucleation and growth on cohesive interfaces, Model. Simulat. Mater. Sci. Eng. 12 (2004) 453–463, https://doi.org/10.1088/0965-0393/12/3/007.
[73] J. Chen, E. Ravey, S. Hallett, M. Wisnom, M. Grassi, Prediction of delamination in braided composite T-piece specimens, Compos. Sci. Technol. 69 (2009) 2363–2367, https://doi.org/10.1016/j.compscitech.2009.01.027.
[74] S. Luo, T. Song, B. Liu, J. Tian, M. Qian, Recent advances in the design and fabrication of strong and ductile (tensile) titanium metal matrix composites, Adv. Eng. Mater. 21 (2019) 1–13, https://doi.org/10.1002/adem.201801331.
[75] Y. Tanaka, J.M. Yang, Y.F. Liu, Y. Kagawa, Characterization of nanoscale deformation in a discontinuously reinforced titanium composite using AFM and nanolithography, Scripta Mater. 56 (2007) 209–212, https://doi.org/10.1016/j.scriptamat.2006.10.015.
[76] S. Wang, L.J. Huang, L. Geng, Y. Sun, H.X. Peng, S.X. Qu, Microstructure evolution and damage mechanism of layered titanium matrix composites under tensile loading, Mater. Sci. Eng. 777 (2020), 139067, https://doi.org/10.1016/j.msea.2020.139067.
[77] N. Chandra, H. Li, C. Shet, H. Ghonem, Some issues in the application of cohesive zone models for metal-ceramic interfaces, Int. J. Solid Struct. 39 (2002) 2827–2855, https://doi.org/10.1016/S0020-7683(02)00149-X.